

EXPERIMENT ATLAS AT THE LHC

PNPI participants of the ATLAS Collaboration: O.L. Fedin, S.V. Katunin, S.V. Kovalenko, N.V. Klopov, L.G. Kudin, V.P. Maleev, A.V. Nadtochi, S.B. Oleshko, S.K. Patrichev, Yu.F. Ryabov, V.A. Schegelsky, E.V. Sedykh, D.M. Seliverstov, V.M. Solovyev, Yu.K. Zalite

1. Introduction

ATLAS is a particle physics experiment at the Large Hadron Collider (LHC) at CERN. The ATLAS detector [1] is searching for new discoveries in the proton-proton collisions of extraordinarily high energy. ATLAS investigates a wide range of physics including searches for the Higgs boson, extra dimensions, and particles that could make up dark matter.

ATLAS is an international collaboration of about 3000 physicists from 174 institutions. PNPI was involved in the ATLAS experiment through the design and construction of the Transition Radiation Tracker (TRT) from the beginning of the conceptual detector design. The TRT is one of three sub-systems of the ATLAS Inner Detector (ID) (Fig. 1), which is composed of the silicon-based Pixel and Semiconductor Tracker (SCT) detectors, and the gaseous drift tube Transition Radiation Tracker. The TRT is the outermost of the three sub-systems.

At present, PNPI physicists participate in the TRT detector operation and in the data analysis including QCD and electroweak physics studies, and heavy bosons searches.

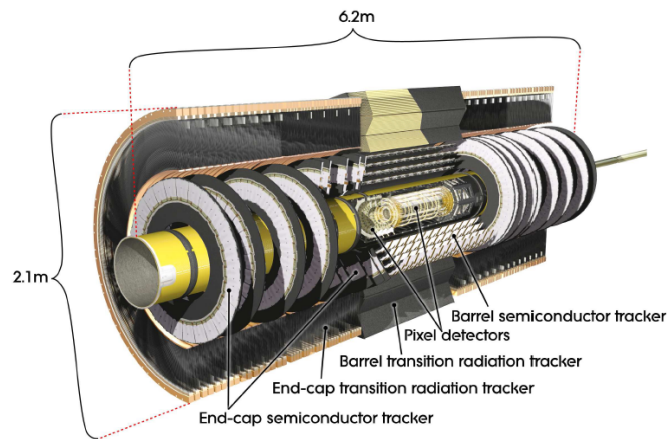


Fig. 1. General view of the Inner Detector of the ATLAS detector

2. Transition Radiation Tracker

The TRT detector was designed for two purposes: extended tracking to provide high resolution of a track transverse momentum measurement and the particle identification based on Transition Radiation (TR). These tasks became possible to realize due to a unique combination of the precision drift time measurement with straws as base elements of the detector, and the registration of soft X -rays emitted by relativistic particles in the radiator filling the space between the straws.

To meet requirements for spatial and momentum resolutions, the initial requirement for the straw hit resolution was set $\sim 170 \mu\text{m}$ with the single straw efficiency $\sim 95\%$ [2]. This should provide $\sim 30 \mu\text{m}$ track resolution in the middle of the detector with ~ 35 measurement points (hits) per track. The TRT makes a crucial contribution to the track measurement. In Fig. 2, the momentum resolution and the impact parameter measurement accuracy obtained in the cosmic ray commissioning performed in 2008–2009 [3] are presented. It is seen that the TRT provides a significant improvement, especially for $p_T > 20 \text{ GeV}/c$. A difference between the simulation and the full ID data indicates mainly remaining intrinsic misalignments. The following alignment [4] has allowed to reach a significant improvement of the spatial resolution. The single

straw hit position resolution of $120\ \mu\text{m}$ for the TRT barrel and $135\ \mu\text{m}$ for the TRT end-caps has been achieved (see Fig. 3).

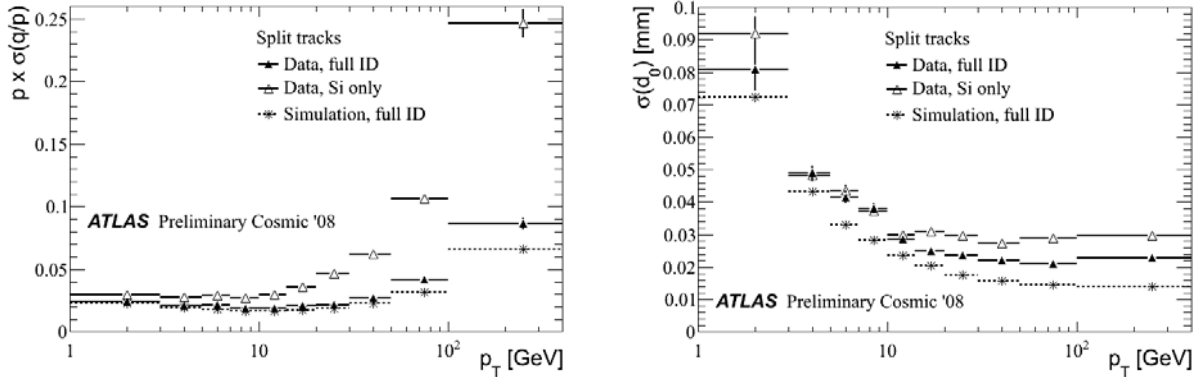


Fig. 2. Momentum resolution (left) and accuracy of the impact parameter measurement (right) as a function of the transverse momentum of the particle. Black dots – simulation, open triangles – combined measurements by the Pixel and SCT detectors, filled triangles – full ID measurement. The difference between simulations and the full ID measurement indicates the remaining misalignment

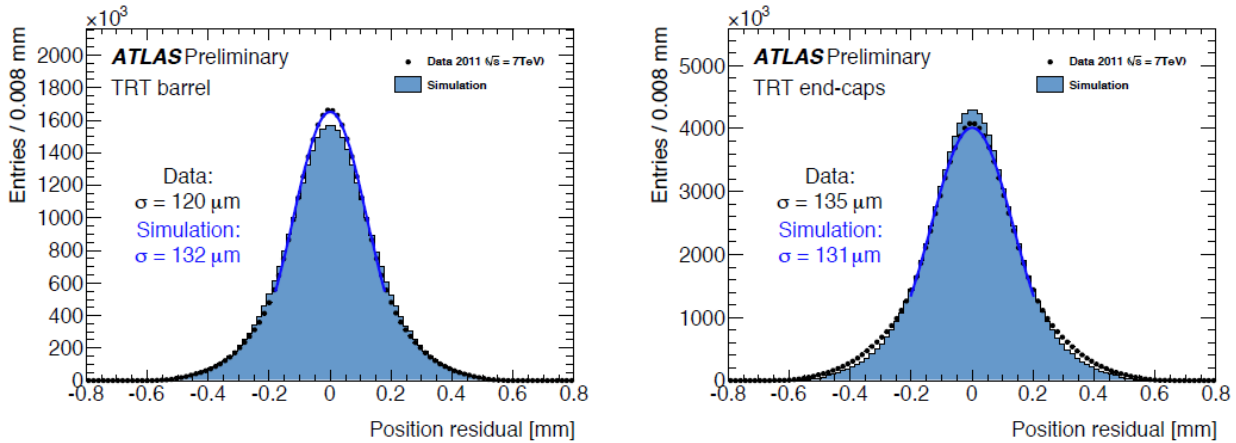


Fig. 3. Single straw spatial resolution after the latest alignment for the TRT barrel (left) and the TRT end-caps (right) obtained with 2011 proton-proton collision data (points) and with simulations (filled histograms)

In addition to its tracking capabilities, the TRT provides discrimination between electrons and pions over the energy range between 1 and 200 GeV by utilizing transition radiation. Transition radiation is emitted when a highly relativistic charged particle with the Lorentz factor $\gamma = E/m \sim 10^3$ traverses boundaries between materials of different dielectric constants. The TR photons (soft X-rays) emitted in the radiator are absorbed in the gas inside straw tubes, which serve as detecting elements both for tracking and for particle identification.

In Fig. 4, the TR photon observation probability depending on the charged particle Lorentz factor (“turn-on” curve) is presented. A pure sample of electrons with high values of γ (above $\gamma = 1000$) is obtained from the data using photon conversions. For low values of γ , all selected tracks in the event are used with an assumption that these particles are pions. As expected, the probability of a high threshold hit increases for particles with the Lorentz factor above 1000, which enables the TRT to separate electrons from pions over a momentum range between 1 GeV/c and 200 GeV/c. It is seen that the onset of TR from the lower plateau (corresponding to the probability of producing high-energy delta-rays) and the upper plateau (corresponding to saturation of the transition radiation production in the geometry chosen for the TRT radiator foils and straw tubes) in the end-cap is steeper than that for the barrel. Small difference between TRT barrel and end-

cups is expected because of different radiator materials used for the barrel (irregularly spaced fibers) and end-caps (regularly spaced foils).

The results agree with those obtained in the minimum bias Monte Carlo simulations for almost all values of the Lorentz factor and provide the TRT detector with an excellent starting point to study and optimize its particle identification properties. The simulation of the transition radiation has so far been tuned on the data collected with the barrel modules only in 2004 on a test beam set-up and can now be improved by using new results from collision data.

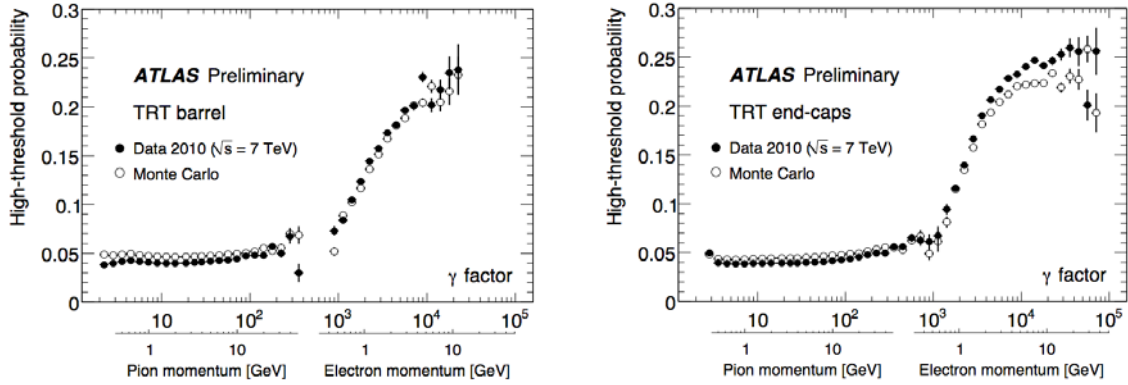


Fig. 4. The probability of a TRT high-threshold hit in the TRT barrel (left) and TRT end-caps (right) as a function of the Lorentz factor γ for the TRT barrel and end-cap regions, as measured in 7 TeV collision events

Another way to distinguish between different types of particles can be based on dE/dx measurements. Though the TRT detector was not designed for this purpose and not equipped with amplitude measuring electronics, discriminators based on TRT timing information can be used for a particle identification since the measured Time over Threshold (ToT) is correlated with the ionization deposit within the straws. For the purpose of dE/dx measurements, the ToT is defined as the number of bits above the threshold in the largest single group of bits above the threshold. Figure 5 shows the ToT distributions for electron and pion candidates (left) and the track-averaged ToT distribution, as a function of the track momenta (right).

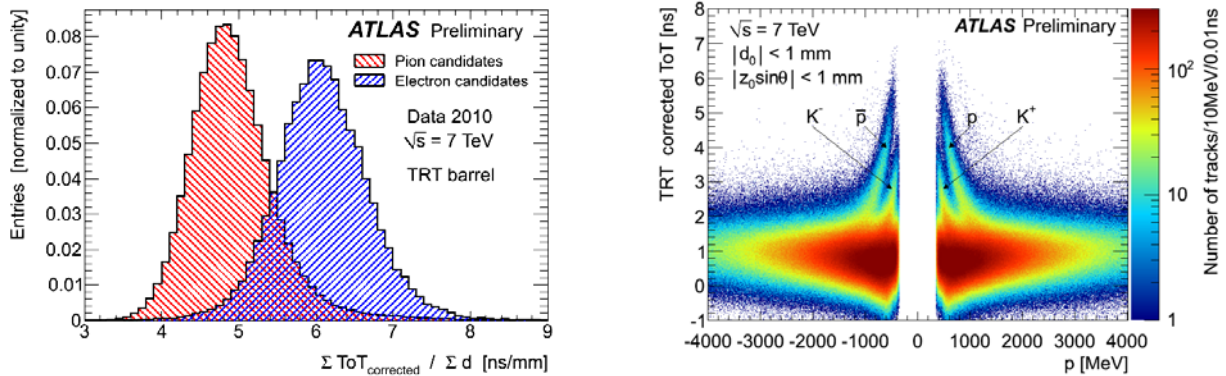


Fig. 5. The average Time over Threshold (ToT corrected), divided by the average transverse track path length inside the straw (left) and the track-averaged ToT distribution, as a function of the track momenta (right)

To compare the performance in collision data with the expected performance reported in the ATLAS Technical Design Report [5], the performance of a selection criterion that gives 90 % electron efficiency is used as a reference. A criterion that gives a 90 % electron efficiency was determined in different momentum bins and applied to the pion sample to determine the efficiency for pions to pass the same criterion. Figure 6 shows the pion misidentification probability $p_{\pi \rightarrow e}$ at 90 % electron efficiency as a function of the momentum. The uncertainties were estimated by varying the selection criteria in such a way that the electron efficiency changed by $\pm 2\%$. It should be noted that any contamination of the pion sample with electrons above

the TR threshold will systematically bias the estimate of $p_{\pi \rightarrow e}$ by roughly the same amount. As seen in Fig. 6, the ToT-based selection improves the pion rejection at $p < 10$ GeV/c [6].

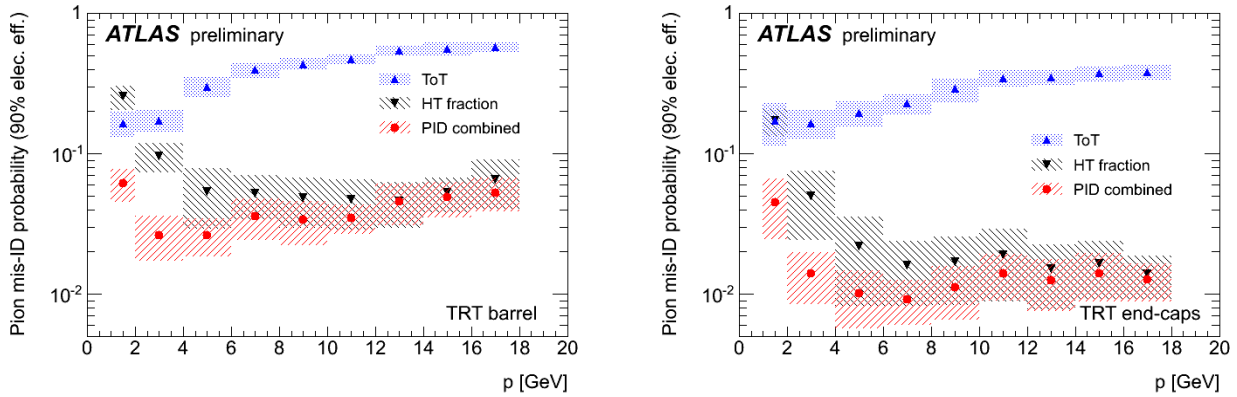


Fig. 6. The pion misidentification probability for a selection criteria that gives 90 % electron efficiency as a function of the momentum for the barrel (left) and end-cap (right) region of the detector

3. Physics results

Figure 7 (left) shows the integrated luminosities recorded by the ATLAS detector during Run I (2010–2012 years data taking periods). In total, ATLAS has recorded data corresponding to about 25 fb^{-1} . ATLAS data taking efficiency was about 94 %. The instantaneous luminosity delivered by the LHC accelerator was increased from $0.5 \cdot 10^{33} \text{ cm}^{-2}\text{s}^{-1}$ in 2010 up to $7.7 \cdot 10^{33} \text{ cm}^{-2}\text{s}^{-1}$ in 2012. It is close to initial design luminosity $10^{34} \text{ cm}^{-2}\text{s}^{-1}$. The average number of interactions per crossing (pile-up) dramatically increases with the luminosity, and it goes rapidly from average 5–7 interaction in 2011 data to 20–25 in 2012 data, as it is shown in Fig. 7 (right). Despite the fact that the ATLAS detector has been nominally designed for lower pile-up (~ 22), the detector performance remained excellent in high pile-up conditions (> 30).

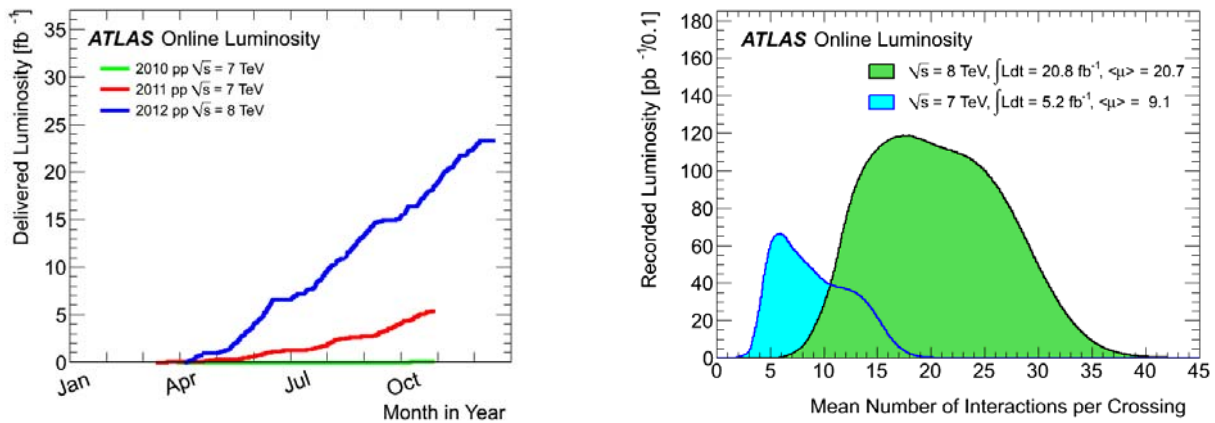


Fig. 7. Integrated luminosity delivered in the ATLAS experiment as a function of time during 2012 (blue), 2011 (red) and 2010 (green) data taking periods (left). The luminosity-weighted distribution of the mean number of interactions per crossing (pile-up) for the 2011 and 2012 data (right)

Using data recorded during Run I, ATLAS has performed a wide range of physics analyses. The major ATLAS result is the discovery of a Higgs-like boson, which is compatible with the Standard Model (SM) Higgs Boson. Unfortunately, no new physics beyond the SM (SUSY, new heavy bosons, *etc.*) has been observed despite great efforts to find it. The predictions of the Standard Model stand firm!

3.1. Discovery of the Higgs boson

The Higgs boson is the only particle of the Standard Model that was not observed previously. During the summer of 2012, both the ATLAS and CMS Collaborations have reported the observation of a Higgs-like particle with a mass of approximately 125 GeV [7, 8]. Note that the electroweak theory does not predict directly the Higgs mass.

SM Higgs analyses with the ATLAS detector were performed for various possible decay modes. The observation of a new boson is well established in the two-photon channel [9], in the four-lepton decay channel [10], as well as in the WW channel [11]. Invariant mass distributions for $H \rightarrow \gamma\gamma$ and $H \rightarrow ZZ \rightarrow 4l$ are shown in Fig. 8.

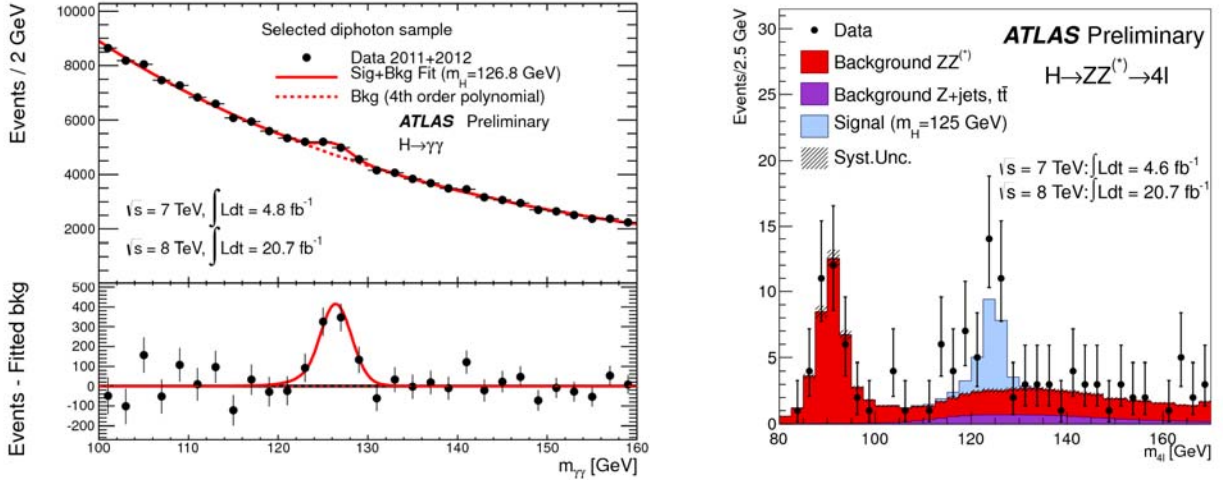


Fig. 8. Invariant mass distribution of diphoton candidates (left) for the combined $\sqrt{s} = 7$ TeV and $\sqrt{s} = 8$ TeV data samples. The result of a fit to the data of the sum of a signal component fixed to $m_H = 126.8$ GeV and a background component described by a fourth-order Bernstein polynomial is superimposed. The distribution of the four-lepton invariant mass (right), for the selected candidates in the four-lepton channel compared to the background expectation for the combined $\sqrt{s} = 8$ TeV and $\sqrt{s} = 7$ TeV datasets. The signal expectation for the $m_H = 125$ GeV hypothesis is also shown (right)

In the $H \rightarrow \gamma\gamma$ decay channel, an excess of events is observed with a local significance of 7σ . The measured mass of the boson is 126.8 ± 0.2 (stat) ± 0.7 (syst) GeV. The signal strength (the ratio of the observed cross section to the expected SM cross section) is $1.65^{+0.24}_{-0.24}$ (stat) $^{+0.25}_{-0.18}$ (syst) for $m_H = 126.8$ GeV, which corresponds to a 2.3σ deviation from the SM prediction. The diphoton invariant mass and the angular distribution of the photons in the resonance rest frame are used to separate the signal and background, and to distinguish between the tested spin hypotheses. The data are in good agreement with the spin-0 hypothesis. The hypothesis of a spin-2 particle produced by gluon fusion is excluded at 99% CL, which corresponds to the expected exclusion.

A clear excess of events over the background is observed with the local significance of 6.6σ in the $H \rightarrow ZZ \rightarrow 4l$ decay channel, corresponding to a background fluctuation probability of $2.7 \cdot 10^{-11}$. The mass of the Higgs-like boson is measured to be $m_H = 124.3^{+0.6}_{-0.5}$ (stat) $^{+0.5}_{-0.3}$ (syst) GeV, and the signal strength at this mass is found to be $1.7^{+0.5}_{-0.4}$. A spin-parity analysis is performed using the events with the reconstructed four-lepton invariant mass satisfying $115 \text{ GeV} < m_{4l} < 130 \text{ GeV}$. The Higgs-like boson is found to be compatible with the SM expectation of 0^+ when compared pair-wise with 0^- , 1^+ , 1^- , 2^+ , and 2^- . The 0^- and 1^+ states are excluded at the 97.8% confidence level or higher using CL's in favour of 0^+ .

The combined measurement [12] of the global signal strength (see Fig. 9, left) for the final states $H \rightarrow \gamma\gamma$, $H \rightarrow ZZ^* \rightarrow 4l$, $H \rightarrow WW^* \rightarrow l\nu l\nu$, $H \rightarrow bb$, and $H \rightarrow \tau\tau$ results in a value of 1.30 ± 0.13 (stat) ± 0.14 (syst) obtained at the mass of 125.5 GeV. The couplings determination of the Higgs-like boson for the three most sensitive channels is shown in Fig. 9 (right).

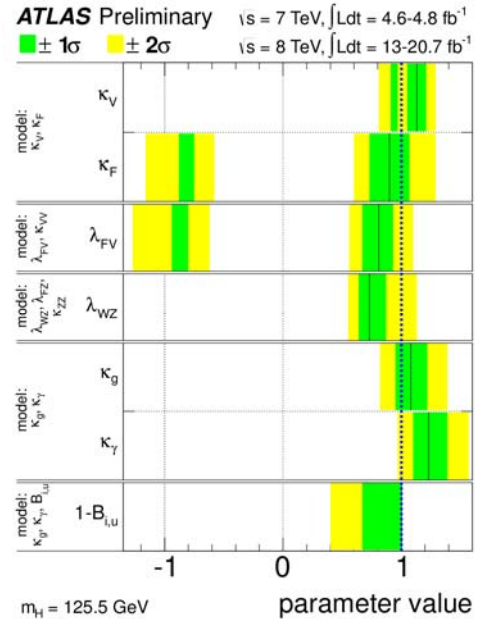
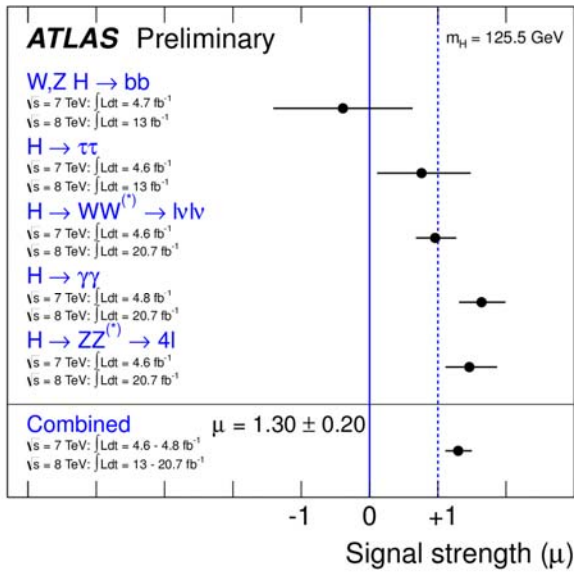


Fig. 9. Measurements of the signal strength parameter (left) at $m_H = 125.5$ GeV for the individual channels and for their combination (left). Summary of the coupling scale factor measurements (right). The best-fit values are represented by the solid vertical line

ATLAS SUSY Searches* - 95% CL Lower Limits

Status: LP 2013

ATLAS Preliminary

$\int \mathcal{L} dt = (4.4 - 22.9) \text{ fb}^{-1}$ $\sqrt{s} = 7, 8 \text{ TeV}$

Model	e, μ, τ, γ	Jets	E_T^{miss}	$\int \mathcal{L} dt [\text{fb}^{-1}]$	Mass limit	Reference	
Inclusive Searches	MSUGRA/CMSSM	1 e, μ	3-6 jets	Yes	20.3	$\tilde{g} \rightarrow b\bar{b}$ 1.2 TeV	any $m(\tilde{g})$
	MSUGRA/CMSSM	0	7-10 jets	Yes	20.3	$\tilde{g} \rightarrow t\bar{t}$ 1.1 TeV	$m(\tilde{t}_1) = 0 \text{ GeV}$
	$\tilde{q}\tilde{q} \rightarrow q\bar{q} + \tilde{g}\tilde{g}$	0	2-6 jets	Yes	20.3	$\tilde{q}\tilde{q} \rightarrow q\bar{q} + \tilde{g}\tilde{g}$ 740 GeV	$m(\tilde{t}_1) = 0 \text{ GeV}$
	$\tilde{g}\tilde{g} \rightarrow q\bar{q} + \tilde{g}\tilde{g}$	0	2-6 jets	Yes	20.3	$\tilde{g}\tilde{g} \rightarrow q\bar{q} + \tilde{g}\tilde{g}$ 1.3 TeV	$m(\tilde{t}_1) = 0 \text{ GeV}$
	$\tilde{g}\tilde{g} \rightarrow q\bar{q} + \tilde{g}\tilde{g}$	1 e, μ	3-6 jets	Yes	20.3	$\tilde{g}\tilde{g} \rightarrow q\bar{q} + \tilde{g}\tilde{g}$ 1.18 TeV	$m(\tilde{t}_1) > 200 \text{ GeV}, m(\tilde{t}_2) = 0.5(m(\tilde{t}_1) + m(\tilde{g}))$
	$\tilde{g}\tilde{g} \rightarrow q\bar{q} + \tilde{g}\tilde{g}$	2 e, μ (SS)	3 jets	Yes	20.7	$\tilde{g}\tilde{g} \rightarrow q\bar{q} + \tilde{g}\tilde{g}$ 1.1 TeV	$m(\tilde{t}_1) > 650 \text{ GeV}$
	GMSB (f NLSP)	2 e, μ	2-4 jets	Yes	4.7	$\tilde{g}\tilde{g} \rightarrow q\bar{q} + \tilde{g}\tilde{g}$ 1.24 TeV	$\tan\beta > 15$
	GMSB (f NLSP)	1-2 τ	0-2 jets	Yes	20.7	$\tilde{g}\tilde{g} \rightarrow q\bar{q} + \tilde{g}\tilde{g}$ 1.4 TeV	$\tan\beta > 15$
	GGM (bino NLSP)	2 γ	0	Yes	4.8	$\tilde{g}\tilde{g} \rightarrow q\bar{q} + \tilde{g}\tilde{g}$ 1.07 TeV	$m(\tilde{t}_1) > 50 \text{ GeV}$
	GGM (wino NLSP)	1 $e, \mu + \gamma$	0	Yes	4.8	$\tilde{g}\tilde{g} \rightarrow q\bar{q} + \tilde{g}\tilde{g}$ 619 GeV	$m(\tilde{t}_1) > 50 \text{ GeV}$
GGM (higgsino-bino NLSP)	7	1 b	Yes	4.8	$\tilde{g}\tilde{g} \rightarrow q\bar{q} + \tilde{g}\tilde{g}$ 900 GeV	$m(\tilde{t}_1) > 200 \text{ GeV}$	
GGM (higgsino NLSP)	2 e, μ (Z)	0-3 jets	Yes	5.8	$\tilde{g}\tilde{g} \rightarrow q\bar{q} + \tilde{g}\tilde{g}$ 690 GeV	$m(\tilde{t}_1) > 200 \text{ GeV}$	
Gravitino LSP	0	mono-jet	Yes	10.5	$\tilde{g}\tilde{g} \rightarrow q\bar{q} + \tilde{g}\tilde{g}$ 645 GeV	$m(\tilde{g}) > 10^{-4} \text{ eV}$	
3rd gen. squarks	$\tilde{g} \rightarrow b\bar{b}$	0	3 b	Yes	20.1	$\tilde{g} \rightarrow b\bar{b}$ 1.2 TeV	$m(\tilde{t}_1) > 600 \text{ GeV}$
	$\tilde{g} \rightarrow t\bar{t}$	0	7-10 jets	Yes	20.3	$\tilde{g} \rightarrow t\bar{t}$ 1.14 TeV	$m(\tilde{t}_1) > 200 \text{ GeV}$
	$\tilde{g} \rightarrow t\bar{t}$	0-1 e, μ	3 b	Yes	20.1	$\tilde{g} \rightarrow t\bar{t}$ 1.34 TeV	$m(\tilde{t}_1) > 400 \text{ GeV}$
	$\tilde{g} \rightarrow b\bar{b}$	0-1 e, μ	3 b	Yes	20.1	$\tilde{g} \rightarrow b\bar{b}$ 1.3 TeV	$m(\tilde{t}_1) > 300 \text{ GeV}$
3rd gen. squarks direct production	$\tilde{t}_1 \tilde{t}_1 \rightarrow b\bar{b}$	0	2 b	Yes	20.1	$\tilde{t}_1 \tilde{t}_1 \rightarrow b\bar{b}$ 100-630 GeV	$m(\tilde{t}_1) > 100 \text{ GeV}$
	$\tilde{t}_1 \tilde{t}_1 \rightarrow b\bar{b}$	2 e, μ (SS)	0-3 b	Yes	20.7	$\tilde{t}_1 \tilde{t}_1 \rightarrow b\bar{b}$ 430 GeV	$m(\tilde{t}_1) > 2 m(\tilde{t}_2)$
	$\tilde{t}_1 \tilde{t}_1 \rightarrow b\bar{b}$	1-2 e, μ	1-2 b	Yes	4.7	$\tilde{t}_1 \tilde{t}_1 \rightarrow b\bar{b}$ 167 GeV	$m(\tilde{t}_1) > 65 \text{ GeV}$
	$\tilde{t}_1 \tilde{t}_1 \rightarrow b\bar{b}$	2 e, μ	0-2 jets	Yes	20.3	$\tilde{t}_1 \tilde{t}_1 \rightarrow b\bar{b}$ 220 GeV	$m(\tilde{t}_1) = m(\tilde{t}_2), m(\tilde{t}_1) - m(\tilde{t}_2) > 50 \text{ GeV}, m(\tilde{t}_1) < m(\tilde{t}_2)$
	$\tilde{t}_1 \tilde{t}_1 \rightarrow b\bar{b}$	2 e, μ (medium), $\tilde{t}_1 \rightarrow b\bar{b}$	0-2 jets	Yes	20.3	$\tilde{t}_1 \tilde{t}_1 \rightarrow b\bar{b}$ 150-440 GeV	$m(\tilde{t}_1) > 0 \text{ GeV}, m(\tilde{t}_1) - m(\tilde{t}_2) > 10 \text{ GeV}$
	$\tilde{t}_1 \tilde{t}_1 \rightarrow b\bar{b}$	0	2 b	Yes	20.1	$\tilde{t}_1 \tilde{t}_1 \rightarrow b\bar{b}$ 150-580 GeV	$m(\tilde{t}_1) > 200 \text{ GeV}, m(\tilde{t}_1) - m(\tilde{t}_2) > 5 \text{ GeV}$
	$\tilde{t}_1 \tilde{t}_1 \rightarrow b\bar{b}$	1 e, μ	1 b	Yes	20.7	$\tilde{t}_1 \tilde{t}_1 \rightarrow b\bar{b}$ 200-610 GeV	$m(\tilde{t}_1) > 0 \text{ GeV}$
	$\tilde{t}_1 \tilde{t}_1 \rightarrow b\bar{b}$	0	2 b	Yes	20.5	$\tilde{t}_1 \tilde{t}_1 \rightarrow b\bar{b}$ 320-660 GeV	$m(\tilde{t}_1) > 0 \text{ GeV}$
	$\tilde{t}_1 \tilde{t}_1 \rightarrow b\bar{b}$	2 e, μ (Z)	1 b	Yes	20.7	$\tilde{t}_1 \tilde{t}_1 \rightarrow b\bar{b}$ 500 GeV	$m(\tilde{t}_1) > 150 \text{ GeV}$
	$\tilde{t}_1 \tilde{t}_1 \rightarrow b\bar{b}$	3 e, μ (Z)	1 b	Yes	20.7	$\tilde{t}_1 \tilde{t}_1 \rightarrow b\bar{b}$ 520 GeV	$m(\tilde{t}_1) = m(\tilde{t}_2) > 180 \text{ GeV}$
EW direct	$\tilde{t}_1 \tilde{t}_1 \rightarrow b\bar{b}$	2 e, μ	0	Yes	20.3	$\tilde{t}_1 \tilde{t}_1 \rightarrow b\bar{b}$ 85-315 GeV	$m(\tilde{t}_1) > 0 \text{ GeV}$
	$\tilde{t}_1 \tilde{t}_1 \rightarrow b\bar{b}$	2 e, μ	0	Yes	20.7	$\tilde{t}_1 \tilde{t}_1 \rightarrow b\bar{b}$ 125-450 GeV	$m(\tilde{t}_1) > 0 \text{ GeV}, m(\tilde{t}_1) > 0.5(m(\tilde{t}_2) + m(\tilde{t}_1))$
	$\tilde{t}_1 \tilde{t}_1 \rightarrow b\bar{b}$	2 τ	0	Yes	20.3	$\tilde{t}_1 \tilde{t}_1 \rightarrow b\bar{b}$ 180-330 GeV	$m(\tilde{t}_1) > 0 \text{ GeV}, m(\tilde{t}_1) > 0.5(m(\tilde{t}_2) + m(\tilde{t}_1))$
	$\tilde{t}_1 \tilde{t}_1 \rightarrow b\bar{b}$	3 e, μ	0	Yes	20.7	$\tilde{t}_1 \tilde{t}_1 \rightarrow b\bar{b}$ 315 GeV	$m(\tilde{t}_1) = m(\tilde{t}_2), m(\tilde{t}_1) > 0, m(\tilde{t}_1) > 0.5(m(\tilde{t}_2) + m(\tilde{t}_1))$
Long-lived particles	Direct $\tilde{t}_1 \tilde{t}_1 \rightarrow b\bar{b}$ prod., long-lived \tilde{t}_1	0	1 jet	Yes	4.7	$\tilde{t}_1 \tilde{t}_1 \rightarrow b\bar{b}$ 220 GeV	$1 - \text{cr}(\tilde{t}_1) < 10 \text{ ns}$
	Stable, stopped \tilde{g} R-hadron	0	1-5 jets	Yes	22.9	$\tilde{g} \rightarrow b\bar{b}$ 857 GeV	$m(\tilde{t}_1) > 100 \text{ GeV}, 10^{-4} \mu\text{s} < \tau(\tilde{g}) < 1000 \text{ s}$
	GMSB, stable \tilde{g}	1-2 μ	0	-	15.9	$\tilde{g} \rightarrow b\bar{b}$ 385 GeV	$5 < \tau_{\text{stop}} < 50$
	Direct $\tilde{t}_1 \tilde{t}_1 \rightarrow b\bar{b}$ prod., stable \tilde{t}_1 or \tilde{t}_2	1-2 μ	0	-	15.9	$\tilde{t}_1 \tilde{t}_1 \rightarrow b\bar{b}$ 395 GeV	$m(\tilde{t}_1) = m(\tilde{t}_2)$
RPV	GMSB, $\tilde{t}_1 \rightarrow \tilde{g}$, long-lived \tilde{t}_1	2 γ	0	Yes	4.7	$\tilde{t}_1 \tilde{t}_1 \rightarrow b\bar{b}$ 230 GeV	$0.4 < \text{cr}(\tilde{t}_1) < 2 \text{ ns}$
	$\tilde{t}_1 \tilde{t}_1 \rightarrow q\bar{q}$ (RPV)	1 μ	0	Yes	4.4	$\tilde{t}_1 \tilde{t}_1 \rightarrow q\bar{q}$ 700 GeV	$1 \text{ mm} < c\tau < 1 \text{ m}, \tilde{g} \text{ decoupled}$
	LFV $pp \rightarrow \tilde{t}_1 + X, \tilde{t}_1 \rightarrow e + \mu$	2 e, μ	0	-	4.6	$\tilde{t}_1 \tilde{t}_1 \rightarrow b\bar{b}$ 1.61 TeV	$A_{111} = 0.10, A_{122} = 0.05$
	LFV $pp \rightarrow \tilde{t}_1 + X, \tilde{t}_1 \rightarrow e(\mu) + \tau$	1 $e, \mu + \tau$	0	-	4.6	$\tilde{t}_1 \tilde{t}_1 \rightarrow b\bar{b}$ 1.1 TeV	$A_{111} = 0.10, A_{122} = 0.05$
Other	Bilinear RPV CMSSM	1 e, μ	7 jets	Yes	4.7	$\tilde{t}_1 \tilde{t}_1 \rightarrow b\bar{b}$ 1.2 TeV	$m(\tilde{g}) = m(\tilde{g}), \text{cr}_{\text{LSP}} < 1 \text{ mm}$
	$\tilde{t}_1 \tilde{t}_1 \rightarrow b\bar{b}$	4 e, μ	0	Yes	20.7	$\tilde{t}_1 \tilde{t}_1 \rightarrow b\bar{b}$ 760 GeV	$m(\tilde{t}_1) > 300 \text{ GeV}, A_{122} > 0$
	$\tilde{t}_1 \tilde{t}_1 \rightarrow b\bar{b}$	3 $e, \mu + \tau$	0	Yes	20.7	$\tilde{t}_1 \tilde{t}_1 \rightarrow b\bar{b}$ 350 GeV	$m(\tilde{t}_1) > 80 \text{ GeV}, A_{122} > 0$
	$\tilde{g} \rightarrow q\bar{q}$	0	6 jets	-	4.6	$\tilde{g} \rightarrow q\bar{q}$ 668 GeV	
Scalar gluon	2 e, μ (SS)	0-3 b	Yes	20.7	$\tilde{g} \rightarrow q\bar{q}$ 880 GeV		
WIMP interaction (D5, Dirac χ)	0	4 jets	-	4.6	$\tilde{g} \rightarrow q\bar{q}$ 100-287 GeV	incl. limit from 1110.2693	
		0	mono-jet	Yes	10.5	$\tilde{g} \rightarrow q\bar{q}$ 704 GeV	$m(\chi) > 80 \text{ GeV}, \text{limit of } 687 \text{ GeV for D8}$

*Only a selection of the available mass limits on new states or phenomena is shown. All limits quoted are observed minus 1σ theoretical signal cross section uncertainty.

Fig. 10. Mass reach of the ATLAS searches for the Supersymmetry. Only a representative selection of the available results is shown

3.2. SUSY searches

The SuperSYmmetry (SUSY) is one of the most promising theories beyond the Standard Model, proposing solutions for some of the most important open questions of the SM, such as the hierarchy problem and unification of the gauge couplings. It also provides a natural cancellation of corrections to the Higgs mass. In addition, this theory provides suitable Dark Matter candidates compatible with astrophysics and astro-particle physics observations such as the WMAP3 measurements of the cosmic microwave background. For these reasons, the search for the SUSY is one of the most important goals of the ATLAS experiment with about 50 different analyses performed in 2011–2012. In the absence of any evidence of the signal, they provide new exclusion limits for various models, such as the minimal SuperGRAvity (mSUGRA), the Gauge-Mediated Supersymmetry Breaking (GMSB), the phenomenological minimal Supersymmetric Standard Model, and others. A summary of the mass limits obtained in the ATLAS SUSY searches is presented in Fig. 10.

3.3. Search of heavy gauge and excited bosons

Although the Standard Model (SM) of strong and electroweak interactions is remarkably consistent with particle physics observations to date, the high-energy collisions at the CERN LHC provide new opportunities to search for physics beyond it. New heavy spin-1 gauge bosons are predicted by many extensions of the SM. They are generically called Z' and W' bosons. The Z' bosons are associated with additional $U(1)'$ gauge symmetries and W' bosons arise in models with an extra $SU(2)$ gauge [13].

In addition to the gauge bosons, another type of spin-1 bosons may exist, which have only a Pauli-like anomalous coupling to fermions instead of the gauge one. This model was proposed by JINR theorists [14]. The anomalous couplings mix both left-handed and right-handed fermions, and therefore these bosons carry a nonzero chiral charge. The associated gauge bosons are labeled as Z^* and W^* . As these bosons are coupled to the tensor quark currents, they can be considered as excited states, and therefore they are also called excited bosons.

PNPI physicists participate in searches of heavy gauge and excited boson, playing a key role in an analysis of decays into the final state with an electron, *i.e.* $Z'/Z^* \rightarrow e^+e^-$ and $W'/W^* \rightarrow ev$. The results presented here use the full data sample recorded by ATLAS in 2011, corresponding to a total integrated luminosity of $\sim 5.0 \text{ fb}^{-1}$.

The event selection and the lepton identification for the process $Z'/Z^* \rightarrow \ell\ell$ are discussed in detail in [15]. Figure 11 shows the invariant mass distribution for the dielectron and dimuon final states after final selections. The expected Z^* signal for three mass hypotheses is shown in Fig. 11. The dilepton invariant mass distributions are well described by the SM. For both channels, the dominant and irreducible background is due to the Z/γ^* (Drell – Yan) process, characterized by the same final state as the signal. Small contributions from $t\bar{t}$ and diboson (WW , WZ and ZZ) production are also present in both channels. Semileptonic decays of b and c quarks into the e^+e^- and $\mu^+\mu^-$ pairs, plus a mixture of photon conversions and hadrons faking electrons in the e^+e^- sample, are backgrounds that are referred to as the QCD background. Jets accompanying W bosons ($W + \text{jets}$) may similarly produce dilepton candidates. The expected signal and backgrounds, with the exception of those from QCD and W^+ jets, are evaluated with simulated samples and are rescaled using the most precise available cross section predictions. The total SM prediction is then normalized to the data in an invariant mass interval around the Z peak ($70\text{--}110 \text{ GeV}/c^2$). In the electron channel, the rescaling is done after adding the QCD multijet and $W + \text{jets}$ backgrounds evaluated directly from the data.

In the absence of a signal, the upper limits on the number of events produced by the decay of a new resonance are determined at the 95% CL. Figure 12 (left) shows the 95% CL for the observed and expected exclusion limits on the combination of the electron and muon channels for Z'_{SSM} and for the lowest and highest value of σB (cross section multiplied by the branching ratio) of the E_6 -motivated Z' models. The rising of the σB limit at very high masses is due to a slight acceptance decrease: contrary to the acceptance as a function of the dilepton masses, which tends to increase at high mass, the acceptance as a function of the

pole mass slightly decreases due to a faster fall of the parton luminosity at very high masses, which distorts the Breit – Wigner resonance shape and enhances the relative contribution of low-mass signal events. The right plot in Fig. 12 shows the 95% CL for the observed and expected exclusion limits on $\sigma B(Z^* \rightarrow \ell^+ \ell^-)$, as well as the value of σB expected from theory. The parameters of the model are fixed by requiring that the total and partial decay widths of W^* , the charged partner of Z^* , should be the same as those of the W'_{SSM} boson with the same mass. As a result, the corresponding 95% CL limits on the mass of the dilepton resonance was set at $2.22 \text{ TeV}/c^2$ for the Z'_{SSM} model and $2.20 \text{ TeV}/c^2$ for the Z^* model. Figure 13 displays the difference between the data and the expectation for both electron and muon channels. Local significance nowhere exceeds two standard deviations. The data are consistent with the SM prediction in this search.

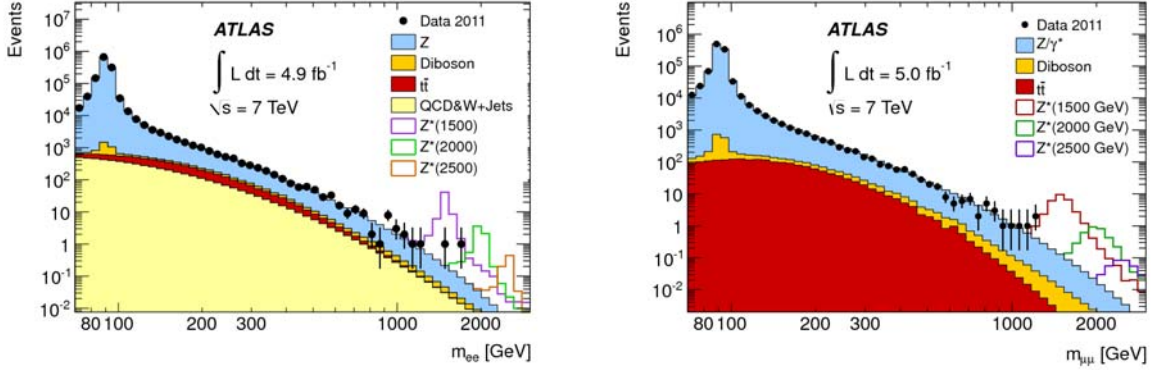


Fig. 11. The dielectron (left) and dimuon (right) invariant mass ($m_{\ell\ell}$) distribution after final selections, compared to the stacked sum of all expected backgrounds, with three example Z^* signals overlaid. The bin width is constant in $\log(m_{\ell\ell})$

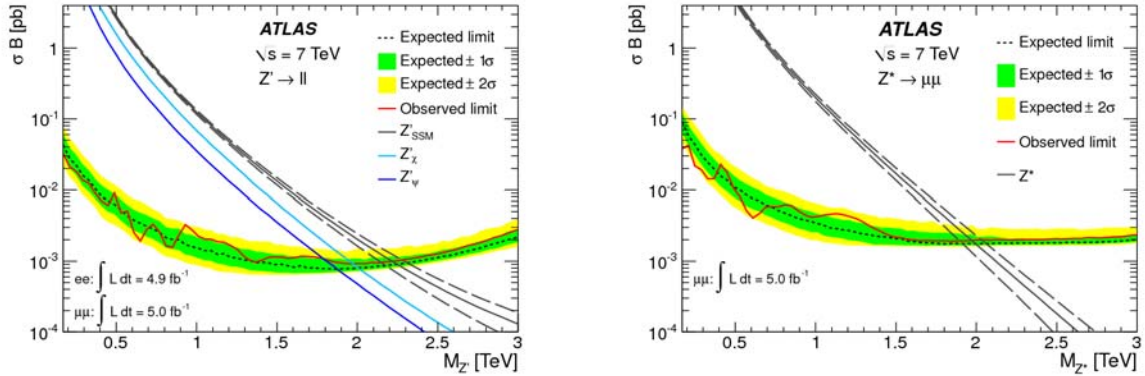


Fig. 12. Expected and observed 95% CL limits on the cross section multiplied by the branching ratio (σB) and the expected value of σB for Z'_{SSM} production and the two E_6 -motivated Z' models with the lowest and highest σB for the combination of the dielectron and dimuon channels (left) and for Z^* boson production for the combination of dielectron and dimuon channels (right). The dashed lines around the Z^* and around the Z'_{SSM} theory curve represent theoretical uncertainties

A search is also performed for the charged partners of Z'/Z^* , denoted as W' and W^* . The event selection and the lepton identification are described in detail in [16]. The same reconstruction and event selection are applied to the data and the simulated samples. Figure 14 shows the m_T spectra for events with $m_T > 200 \text{ GeV}/c^2$ in each channel after the event selection. The data, the expected background, and three examples of W' signals at different masses are shown. The main background to the $W'/W^* \rightarrow l\nu$ signal comes from the high- m_T tail of the SM W boson decay to the same final state. Other backgrounds are Z bosons decaying into two leptons where one lepton is not reconstructed, W or Z decaying to τ -leptons where a τ subsequently decays to an electron or muon, and diboson production. These are collectively referred to as the electroweak background. In addition, there is a background contribution from $t\bar{t}$ and single-top production which is most important for the lowest W'/W^* masses considered here, where it constitutes about 15 % of the background after the event selection. Other strong-interaction background sources, where a light or heavy

hadron decays semileptonically or a jet is misidentified as an electron or muon, are estimated from the data to be 10 % at most of the total background in the electron channel and a negligible fraction in the muon channel. These are called QCD background.

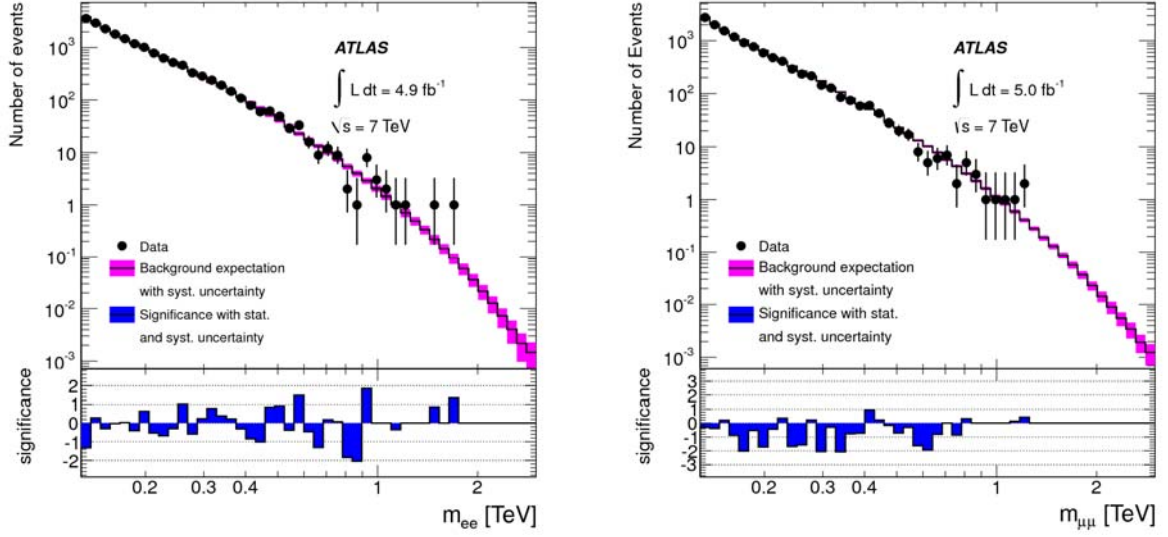


Fig. 13. Differences between data and expectation in the electron (left) and muon (right) channels. The mass range goes from 128 GeV/c^2 to 3 TeV/c^2 . Both statistical and systematic uncertainties have been taken into account

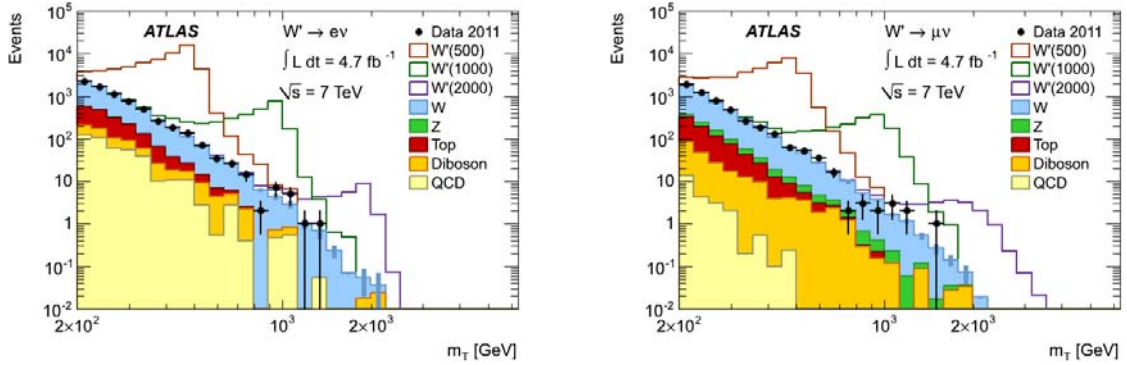


Fig. 14. Spectra of m_T for the electron (left) and muon (right) channels for events with $m_T > 200 \text{ GeV}/c^2$ after event selection. The points represent the data, and the filled histograms show the stacked backgrounds. Open histograms for $W'/W^* \rightarrow l\nu$ signals added to the background with masses in GeV are indicated in parentheses in the legend. The QCD backgrounds estimated from the data are also shown. The signal and other background samples are normalized using the integrated luminosity of the data and the NNLO cross sections

The σB limits are evaluated independently for both W' and W^* . The observed number of events N_{obs} is the count after the final selection including the requirement $m_T > m_T^{\text{min}}$, with the thresholds chosen separately for each of the masses and decay channels to maximize the sensitivity. None of the observations for any mass in either channel or their combination has a significance above three standard deviations, so there is no evidence for the observation of $W' \rightarrow l\nu$ or $W^* \rightarrow l\nu$ decays. Figure 15 presents the 95% CL observed for the combined limits on σB for both $W' \rightarrow l\nu$ and $W^* \rightarrow l\nu$. A W' boson with the Sequential SM couplings is excluded at the 95 % credibility level for masses up to 2.55 TeV/c^2 . Excited chiral bosons (W^*) with the equivalent coupling strength are excluded for masses up to 2.42 TeV/c^2 .

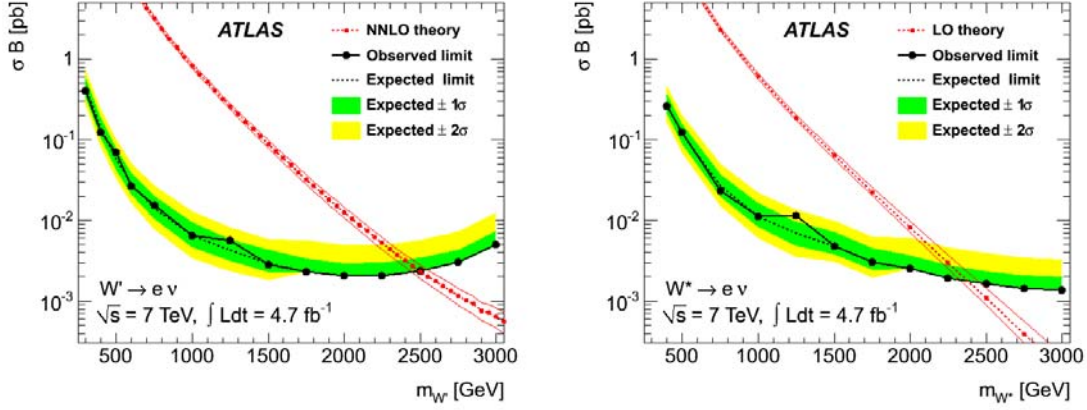


Fig. 15. Expected and observed combined limits on σB for $W' \rightarrow l\nu$ (left) and $W^* \rightarrow l\nu$ (right) obtained by assuming the same branching fraction for both channels. The NNLO calculated cross section and its uncertainty are also shown

3.4. Observation of inclusive electrons

A precise measurement of inclusive electrons production at the LHC could lead to quantitative comparisons with theory for the production of charm and beauty hadrons. It is also required to understand the basic processes which will be the main sources of backgrounds to measurements and searches involving one electron with high transverse energy E_T in the final state, in particular the observation and early measurements of $W \rightarrow e\nu$ decays and, at a somewhat later stage, of semileptonic decays of top quarks and possible signals from decays of supersymmetric particles.

PNPI physicists participate in developing and validation of electron reconstruction and identification algorithms. These algorithms are designed to achieve both a large background rejection and a high and uniform efficiency for isolated electrons over the full acceptance of the detector, for transverse energies above 20 GeV. These electrons need to be separated from hadrons in QCD jets and from secondary electrons originating mostly from photon conversions in the tracker material. The baseline electron identification algorithm in ATLAS relies on variables which deliver good separation between isolated electrons and fake signatures from QCD jets. These variables include information from the calorimeter, the tracker, and matching between the tracker and the calorimeter. The TRT detector built at PNPI as a part of the ATLAS tracker provides a substantial discriminating power between electrons and pions over a wide energy range between 0.5 and 100 GeV.

Based on an integrated luminosity of 13.8 nb^{-1} obtained with stable beams and very loose electron trigger requirements, the properties of a total of 67124 electron candidates with $E_T > 7 \text{ GeV}$ and $|\eta| < 2.0$ passing an optimized set of identification cuts was studied [17]. The preselection requires that the electron candidates lie within the pseudorapidity coverage of the TRT, $|\eta| < 2.0$, and outside the transition region between the barrel and end-cap calorimeters, $1.37 < |\eta| < 1.52$. Only reconstructed electron candidates with a raw cluster transverse energy above 4 GeV and a calibrated offline cluster transverse energy above 7 GeV are considered. This choice is the result of a balance between the high statistics required for the analysis and the requirement of a high and uniform trigger efficiency. The preselected electrons are also required to be associated to tracks containing at least ten TRT hits and four hits in the Pixel and SCT detectors. Preselected electron candidates were selected further using the medium identification criteria, which consist of requirements on their energy deposits in the strip layer of the ElectroMagnetic (EM) calorimeter and on the track quality and the track-cluster matching. Figure 16 displays the transverse energy and pseudorapidity spectra for these electron candidates. The prompt electrons comprise mostly non-isolated electrons from the charm and beauty hadron decay in this low-energy range, and only a very small fraction of them is expected to be isolated electrons from W/Z -boson decay. The distributions were compared between the data and simulations. The Monte Carlo distributions are normalized to the same number of electron candidates passing the medium identification criteria as in the data. The transverse energy and pseudorapidity spectra of the signal are in agreement in shape between the data and predictions from leading-order parton shower

Monte Carlo simulations (Fig. 16). The breakdown of electron candidates in the Monte Carlo simulation according to their origin is the following: $69.6 \pm 0.1\%$ hadrons, $20.2 \pm 0.2\%$ secondary electrons (conversions), and $10.1 \pm 0.1\%$ prompt electrons.

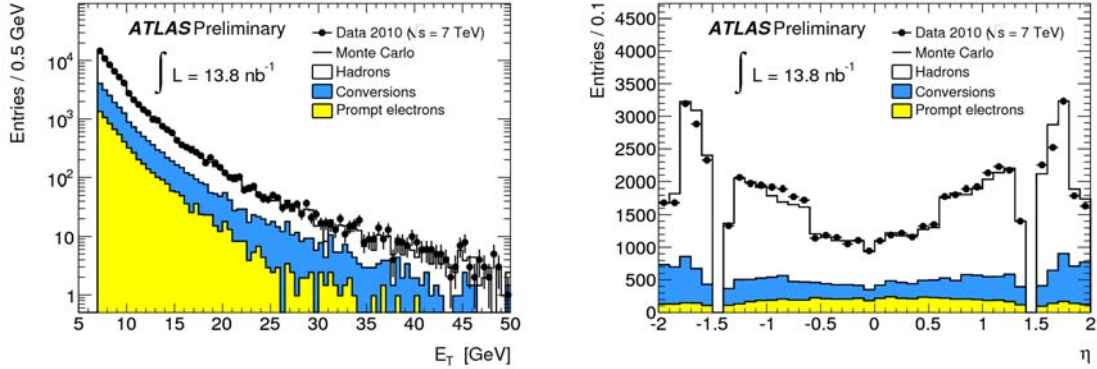


Fig. 16. Distributions of cluster transverse energy E_T (left), and pseudorapidity η (right), for electron candidates passing the medium identification cuts

A signal of 9920 ± 160 (stat.) ± 990 (syst.) electrons, predominantly from heavy flavour production, is measured within this sample. Further analysis is required to extract differential cross-sections for production of electrons from heavy flavour at the LHC.

3.5 Bose – Einstein correlation parameters from the ATLAS experiment

One of the ways to study the space-time picture of hadronic interaction is to measure correlations between two identical particles which momenta are close to each other – the so called Bose – Einstein Correlations (BEC). The general definition of a correlation function for two variables p_1 and p_2 can be written as

$$C_2(p_1, p_2) = \frac{P(p_1, p_2)}{P_{ref}(p_1, p_2)},$$

where $P(p_1, p_2)$ is the probability to observe particles with the momenta p_1 and p_2 . The proximity in the phase space between final state particles with 4-momenta p_1 and p_2 can be quantified by $Q^2 = (p_1 - p_2)^2$. The BEC effect is observed as an enhancement at low Q values, $Q \sim 300$ MeV. To extract the effect one can compare the measured Q -spectra with the reference ones without BEC. Then the ratio

$$R(Q) = \frac{\frac{dN}{dQ} - \frac{dN_{ref}}{dQ}}{\frac{dN_{ref}}{dQ}}$$

can be fitted with an appropriate formula $R(Q) = F(rQ) + a + bQ$. Here, $F(rQ)$ is the Fourier transform of the spatial distribution of the emission region with an effective size $\langle r \rangle$. The function $F(rQ)$ can be parameterized as a linear exponent $F(rQ) = C \cdot \exp(-r_e Q)$ or a Gaussian $F(rQ) = C \cdot \exp(-r_g^2 Q^2)$. For the same value of $\langle r \rangle$, there is quite a simple relation between these two cases: $r_e = \pi^{1/2} r_g$.

ATLAS has collected large event samples of multi-particles production at low intensity LHC runs with beam energies 2.76 and 7 TeV. The number of collisions was ~ 1 per beam crossing. Under such conditions it is possible to make precise measurements of QCD processes. The size of the particle radiation zone was determined from the observed Bose – Einstein correlation (Fig. 17). As it was predicted by Gribov – Regge theory, the interaction radius is slowly rising with the energy. At the same time, the size of the radiation zone at moderate multiplicities depends only from the multiplicity, and its rise with the energy is connected with the multiplicity increase. Such a rise should be limited because of a finite radius of the colliding particles. In

the runs with the beam energy 2.76 TeV, a special trigger was implemented to collect events with high multiplicities in the final state. It occurs that the radius rise is saturated indeed at high multiplicities and this saturation happens at a higher value of the multiplicity as soon as the beam energy increases. Such an effect has been observed for the first time in the ATLAS data.

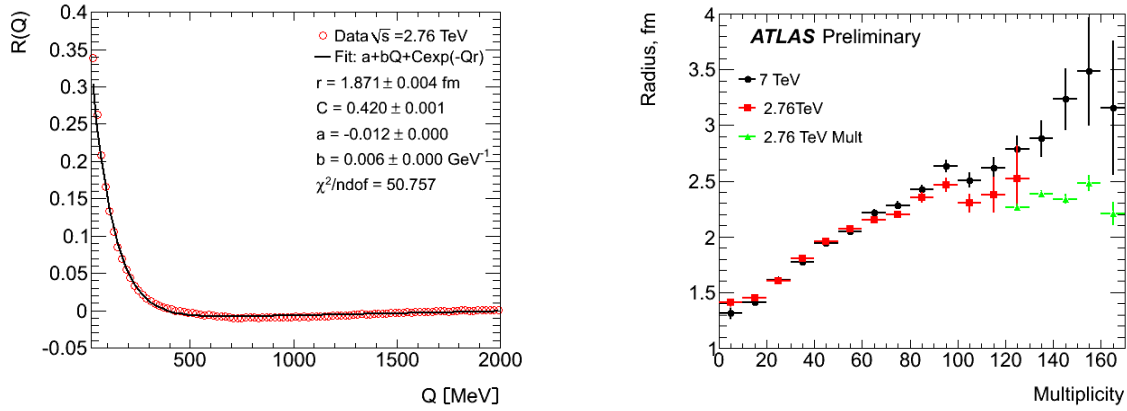


Fig. 17. Bose – Einstein correlation parameters from the ATLAS experiments. The measured value of $R(Q)$ for 2.76 TeV data (left). The radiation zone radius $r = \langle r \rangle$ as a function of the multiplicity (right). The data obtained with a special trigger to collect high multiplicity events at the beam energy 2.76 TeV are shown in green colour

4. Summary

The ATLAS experiment successfully operated during Run I (2010–2012). The ATLAS detector was working well with a high data taking efficiency $\sim 97\%$. A number of physics results have been obtained these years, which have been published in about 240 papers and many more in the pipeline. Only a part of the collected data has been analysed. The data analysis will be continued till the new start-up of the LHC in 2015.

The discovery of a Higgs boson with the mass of ~ 125 GeV was a great result for the more than 20 years old LHC project. Now we should answer the question – is this the Minimal Standard Model Higgs? Answering this question will take time and will require to measure more precisely as many characteristics of the Higgs boson as possible. With the Higgs mass known, the MSM couplings can now be calculated and compared with the experimental results. The SUSY theory is also affected by the Higgs discovery. The measured value of the Higgs mass at the LHC may give indirect evidence for the existence of different SUSY scenarios. With the new LHC physics run in 2015, there will be another round of searches for SUSY and other “new physics”.

According to the plans, the LHC and the ATLAS detector in 2018 will undergo the Phase-1 upgrade to the full energy (14 TeV) and to the design luminosity – $2 \times 10^{34} \text{ s}^{-1} \text{ cm}^{-2}$ with 25 ns bunch spacing. In the physics run which will follow, ATLAS will record about 350 fb^{-1} of data. It has been estimated that with $\sim 300 \text{ fb}^{-1}$ of data, the spin-parity of Higgs will be known to $\sim 5 \sigma$ level, and the ratios of couplings will be known to within 30–50 %. PNPI will take an active part in this upgrade program.

There is a possibility that with an increase of the pp collision energy from 8 TeV to 13 TeV in 2015, we will cross a threshold above which we will observe new particles, too heavy to have been observed so far. This would be really interesting.

References

1. ATLAS Collaboration, G. Aad *et al.*, *The ATLAS Experiment at the CERN Large Hadron Collider*, JINST **3**, S08003 (2008).
2. ATLAS Collaboration, G. Aad *et al.*, *Atlas Inner Detector Technical Design Report. 1*, ATLAS TDR **4**, CERN-LHCC-97-16, CERN (1997).
3. ATLAS Collaboration, G. Aad *et al.*, *The ATLAS Inner Detector Commissioning and Calibration*, Eur. Phys. J. C **70**, 787 (2010).
4. ATLAS Collaboration, G. Aad *et al.*, *Alignment of the ATLAS Inner Detector Tracking System with 2010 LHC Proton-Proton Collisions at $\sqrt{s} = 7$ TeV*, ATLAS-CONF-2011-012, CERN (2011).
5. ATLAS Collaboration, G. Aad *et al.*, *ATLAS Detector and Physics Performance: Technical Design Report, 1*, ATLAS Note CERN-LHCC-99-014.
6. ATLAS Collaboration, G. Aad *et al.*, *Particle Identification Performance of the ATLAS Transition Radiation Tracker*, ATLAS-CONF-2011-128, CERN (2011).
7. ATLAS Collaboration, G. Aad *et al.*, *Observation of a New Particle in the Search for the Standard Model Higgs Boson with the ATLAS Detector at the LHC*, Phys. Lett. B **716**, 1 (2012).
8. CMS Collaboration, S. Chatrchyan *et al.*, *Observation of a New Boson at a Mass of 125 GeV with the CMS Experiment at the LHC*, Phys. Lett. B **716**, 1 (2012).
9. ATLAS Collaboration, G. Aad *et al.*, *Measurements of the Properties of the Higgs-Like Boson in the Two Photon Decay Channel with the ATLAS Detector Using 25 fb⁻¹ of Proton-Proton Collision Data*, ATLAS-CONF-2013-012, CERN (2013).
10. ATLAS Collaboration, G. Aad *et al.*, *Measurements of the Properties of the Higgs-Like Boson in the Four Lepton Decay Channel with the ATLAS Detector Using 25 fb⁻¹ of Proton-Proton Collision Data*, ATLAS-CONF-2013-013, CERN (2013).
11. ATLAS Collaboration, G. Aad *et al.*, *Measurements of the Properties of the Higgs-Like Boson in the $WW^{(*)} \rightarrow \ell\nu\ell\nu$ Decay Channel with the ATLAS Detector Using 25 fb⁻¹ of Proton-Proton Collision Data*, ATLAS-CONF-2013-030, CERN (2013).
12. ATLAS Collaboration, G. Aad *et al.*, *Combined Coupling Measurements of the Higgs-Like Boson with the ATLAS Detector Using up to 25 fb⁻¹ of Proton-Proton Collision Data*, ATLAS-CONF-2013-034, CERN (2013).
13. D. London and J. L. Rosner, *Extra Gauge Bosons in E(6)*, Phys. Rev. D **34**, 1530 (1986).
14. M. Chizhov, V. Bednyakov, and J. Budagov, *Proposal for Chiral-Boson Search at LHC via Their Unique New Signature*, Phys. At. Nucl. **71**, 2096 (2008).
15. ATLAS Collaboration, G. Aad *et al.*, *Search for High-Mass Resonances Decaying to Dilepton Final states in pp Collisions at $\sqrt{s} = 7$ TeV with the ATLAS Detector*, arXiv:1209.2535.
16. ATLAS Collaboration, G. Aad *et al.*, *ATLAS Search for a Heavy Gauge Boson Decaying to a Charged Lepton and a Neutrino in pp Collisions at $\sqrt{s} = 7$ TeV*, arXiv:1209.4446.
17. ATLAS Collaboration, G. Aad *et al.*, *Observation of Inclusive Electrons in the ATLAS Experiment at $\sqrt{s} = 7$ TeV*, ATLAS-CONF-2010-073.